

Direct Deep Neural-network Extraction of Generalized Parton Distributions

Dima Watkins^{1,*} and Dustin Keller^{1,†}

¹*Department of Physics, University of Virginia, Charlottesville, USA*

(Dated: December 29, 2025)

We present a machine-learning method for the nonparametric extraction of generalized parton distributions (GPDs) from Compton form factors (CFFs) constrained by experimental data. The method addresses the longstanding inverse problem posed by the principal-value (PV) linear integral transform with a singular kernel that relates the charge-conjugation-even (C-even) quark GPD $H^{(+)}$ to the real part of the deeply-virtual Compton scattering (DVCS) amplitude. Our approach constructs a differentiable representation of the Quantum Chromo-dynamics (QCD) PV kernel and embeds it as a fixed, physics-preserving layer inside a neural network that parameterizes the GPD $H^{(+)}(x, \xi, t, Q^2)$ itself. The model enforces exact oddness in x , implements endpoint suppression, and includes curvature-based regularization that stabilizes the inversion in kinematically ill-conditioned regions. A Monte-Carlo ensemble of CFFs, obtained from a global neural-network fit to unpolarized DVCS measurements with propagated experimental uncertainties, serves as input to a replica ensemble of GPD networks, yielding a fully probabilistic extraction of $H^{(+)}$ over the phase space. We demonstrate the method using a global determination of $\Re \mathcal{H}$ for Jefferson Lab measurements, and present a direct neural network reconstruction of three-dimensional GPD surfaces $H^{(+)}(x_0, \xi, t, Q_0^2)$ obtained from experimental CFF inputs. This work establishes a flexible, scalable, and model-independent strategy for extracting multidimensional hadronic structure from current and future DVCS data and other GPD related processes.

I. INTRODUCTION

Understanding the multidimensional quark and gluon structure of the nucleon is a central goal of contemporary hadronic physics. Generalized parton distributions (GPDs), introduced more than two decades ago, provide a unified framework that simultaneously characterizes the longitudinal momentum, transverse spatial structure, and spin-orbit correlations of quarks and gluons inside hadrons [1–4]. In deeply-virtual Compton scattering (DVCS), the quark GPDs enter through Quantum Chromo-dynamics (QCD) factorization theorems that connect the nonperturbative nucleon structure to the experimentally measurable Compton form factors (CFFs) [5–7]. The real part of the dominant CFF, $\Re \mathcal{H}$, is expressed as a singular principal-value (PV) linear integral transform with a singular kernel of the charge-conjugation-even (C-even) quark GPD $H^{(+)}(x, \xi, t, Q^2)$, which makes the inversion problem fundamentally ill-posed [8, 9]. In practice, this linear integral transform smears localized x -space information across broad regions of ξ and t , causing substantial degeneracy when reconstructing the underlying GPD directly from experimental CFF data [10–12].

Traditional GPD extractions rely on functional parametrizations incorporating double-distribution models, Regge behaviors, positivity constraints, or assumptions about polynomiality and Q^2 evolution [13–15]. While successful, these methods inevitably introduce model dependence, and their functional rigidity can obscure the true uncertainty associated with the inverse mapping. More recently, machine-learning (ML) approaches

have been explored to reduce this bias, most notably in global CFF neural-network analyses of DVCS cross sections and asymmetries [16–19]. A milestone in the field applying ML to problems of nucleon structure was the extraction of parton distribution functions (PDFs) — probability distribution functions arising as the forward limit of GPDs and describing longitudinal momentum distribution of partons in a nucleon — using artificial neural-networks (ANNs), the project of which is known as NNPDF [20–25]. An important step toward ANN modeling of GPDs themselves was taken in Ref. [26]; therein, the authors constructed effectively nonparametric GPD model constrained by polynomiality [27–30], a requirement imposed by Lorentz invariance, and positivity [30–39], reflecting a properly-normed state in the Hilbert space of states, using pseudo-data generated from phenomenological models. However, in all of these strategies, the GPD-to-CFF integral transform enters only as an external ingredient (through model calculations or post-processing), rather than as an intrinsic component of the learning architecture. Additionally, none of the previously-cited references perform a direct nonparametric inversion of the PV kernel on experimental CFF ensembles, as we propose here.

In this work, we introduce a new approach — the *differentiable PV inversion method* — in which the QCD integral transform that maps $H^{(+)}$ to $\Re \mathcal{H}$ is implemented as a fixed, analytic, differentiable operator inside a neural network. This design has several key advantages. First, the network outputs the GPD itself, given CFF input information, which enforces the exact oddness $H^{(+)}(x) = -H^{(+)}(-x)$ and the expected endpoint behavior through a compact envelope function $(1 - |x|)^\beta$. Here, the CFF ($\Re \mathcal{H}$) input information is provided by a DNN model, continuous in a region of phase space, defined by (x_b, t, Q^2) , obtained from a global fit [40] to experimen-

* bem8mq@virginia.edu

† dustin@virginia.edu

tal DVCS data using the BMK formalism [41]. Second, curvature-based regularization is applied directly in the GPD domain, stabilizing the inversion by suppressing spurious oscillations in x , ξ , and t that would otherwise be amplified by the PV kernel. Third, the integral transform is computed on a high-resolution x grid in a manner that is fully differentiable, enabling gradient-based training needed for our modern deep-learning approach.

To quantify the uncertainties propagated from the experimental data, we train a replica ensemble in PyTorch [42] across an ensemble of replicas of the CFF obtained from a global fit, where many local CFF fits were used to construct a deep neural network (DNN) model over a range of kinematics to make a continuous mapping across phase space [40]. The resulting ensemble yields both a mean prediction and a pointwise uncertainty band for $H^{(+)}(x, \xi, t, Q^2)$ at any desired kinematic point accessible within the grid, without imposing a factorized or truncated functional form. Because the principal-value integral operator is implemented natively as a differentiable layer within the network, the method is readily extendable. As such, we are using $H^{(+)}(x, \xi, t, Q^2)$ and $\text{Re}\mathcal{H}$ only as an illustrative example in this first study.

With upcoming high-precision DVCS measurements from Jefferson Lab (JLab) and the Electron-Ion Collider (EIC) [43–46], the need for flexible, model-independent, uncertainty-quantified GPD extractions is more urgent than ever. The methodology introduced here provides a robust, scalable solution to this inverse problem and opens a new path toward precision nucleon tomography from experimental data alone. The remainder of this paper is organized as follows: In Section II, we review the relation between CFFs and GPDs and the structure of the PV integral transform; Section III introduces the differentiable PV inversion and neural-network architecture; Section IV describes the numerical implementation and replica workflow; Section VI presents our results; and Section VII contains a discussion and outlook.

II. COMPTON FORM FACTORS AND THEIR RELATION TO GPDs

The DVCS process, $eN \rightarrow eN\gamma$, provides a clean probe of the quark and gluon structure of the nucleon through

the nonforward quark correlators known as generalized parton distributions (GPDs) [1–3]. In the Bjorken regime,

$$Q^2 \equiv -q^2 \gg \Lambda_{\text{QCD}}^2, \quad x_B = \frac{Q^2}{2p \cdot q} = \frac{2\xi}{1+\xi}, \quad |t| \ll Q^2, \quad (1)$$

DVCS amplitudes factorize into perturbatively calculable coefficient functions and nonperturbative GPDs, according to the QCD factorization theorems of Refs. [5–7]. The leading-twist quark contribution to the DVCS amplitude is expressed in terms of the four complex-valued CFFs \mathcal{H} , \mathcal{E} , $\tilde{\mathcal{H}}$, and $\tilde{\mathcal{E}}$, which encode the nonperturbative structure of the nucleon.

In this work we focus on the CFF \mathcal{H} as a demonstration of our method. Throughout, we restrict ourselves to the leading-twist quark contribution at leading order in α_s , neglecting gluon GPDs, higher-twist corrections, and any possible subtraction constant (D-term) in the dispersion relation for \mathcal{H} . Under these simplifications, \mathcal{H} is given by the integral [5]

$$\mathcal{H}(\xi, t, Q^2) \Big|_{\text{LO}} = \sum_q e_q^2 \int_{-1}^1 dx \left[\frac{1}{x - \xi + i0} + \frac{1}{x + \xi - i0} \right] H_q(x, \xi, t, Q^2), \quad (2)$$

where e_q is the quark electric charge in units of e . Using the standard distribution identity $(x \pm i0)^{-1} = \text{PV}(1/x) \mp i\pi\delta(x)$, we obtain the imaginary and real parts of the CFF. The expression in brackets in Eq. (2) is the hard-scattering kernel, which arises from the quark propagator in the handbag diagram [7, 12].

It is convenient to introduce the C-even quark GPDs,

$$H_q^{(+)}(x, \xi, t, Q^2) = H_q(x, \xi, t, Q^2) - H_q(-x, \xi, t, Q^2), \quad (3)$$

so that the quark contribution to the CFF can be written as $\mathcal{H} = \sum_q e_q^2 \mathcal{H}_q$ with \mathcal{H}_q expressed in terms of $H_q^{(+)}$. Because the C-even GPD $H_q^{(+)}(x, \xi, t, Q^2)$ is odd in x , the quark-level convolution may be restricted without loss of generality to the interval $x \in [0, 1]$. Applying the

standard distribution identity

$$\frac{1}{x \pm i0} = \text{PV} \left(\frac{1}{x} \right) \mp i\pi\delta(x),$$

to the hard-scattering denominators in Eq. (2), and using the definition of the C-even combination, one obtains the

familiar expressions for the imaginary and real parts of the CFF $\mathcal{H}(\xi, t, Q^2)$ [16, 47–49]:

$$\Im m \mathcal{H}(\xi, t, Q^2) = -\pi \sum_q e_q^2 H_q^{(+)}(x = \xi, \xi, t, Q^2), \quad (4)$$

$$\Re e \mathcal{H}(\xi, t, Q^2) = \text{PV} \int_0^1 dx \left[\frac{1}{\xi - x} - \frac{1}{\xi + x} \right] H^{(+)}(x, \xi, t, Q^2), \quad (5)$$

where we have introduced the charge-weighted C-even GPD $H^{(+)} \equiv \sum_q e_q^2 H_q^{(+)}$, so that the sum over quark flavors is implicit in Eq. (5).

Equation (5) defines a singular Hilbert-transform-type integral. As a consequence, the real part of the CFF is a linear principal-value integral transform of the underlying GPD, and its inversion constitutes a genuinely ill-posed problem: localized features of $H^{(+)}(x, \xi, t, Q^2)$ are smeared over a broad range of ξ and t , and small perturbations in the CFF can induce large variations in the reconstructed GPD.

A. Kinematic structure of the convolution

The variable ξ controls the longitudinal momentum transfer in the t -channel, while x represents the average light-cone momentum fraction carried by the struck quark relative to its parent hadron. The domain splits naturally into:

- the DGLAP region, $x > \xi$, describing quark emission and reabsorption;
- the ERBL region, $x < \xi$, describing quark-antiquark pair creation.

The PV kernel in Eq. (5) diverges at $x = \xi$, which gives rise to the δ -function contribution in $\Im m \mathcal{H}$ and makes $\Re e \mathcal{H}$ highly sensitive to the local curvature of $H^{(+)}$ near this point [7, 12]. As ξ increases for fixed t and Q^2 , the ERBL region $0 < x < \xi$ expands and the integral transform increasingly smears information about the underlying x -dependence of the GPD, reflecting the dominance of the quark-antiquark ($q\bar{q}$) configuration in this domain [10, 12]. Conversely, at small ξ the kernel becomes sharply peaked around $x = \xi$, so that the inverse problem behaves like a Hilbert transform with a strongly ill-conditioned kernel; small perturbations in the CFF then induce large variations in $H^{(+)}$ unless the GPD is controlled by appropriate smoothness priors [9, 50].

B. Mathematical structure and ill-posedness

The mapping

$$H^{(+)}(x, \xi, t, Q^2) \longrightarrow \Re e \mathcal{H}(\xi, t, Q^2) \quad (6)$$

is a Fredholm equation of the first kind with a singular kernel. Such transforms are known to be ill-posed [9]: Small perturbations in the CFF can correspond to large variations in the underlying GPD, so the inverse mapping is highly sensitive to noise in the CFF data. Regularization is therefore essential. Analytically, polynomiality and dispersion relations constrain GPD moments, but they do not guarantee a unique or stable pointwise inversion of Eq. (5). Numerically, the PV integral transform behaves similarly to a Hilbert transform, which amplifies high-frequency components unless the GPD is controlled with smoothness priors.

C. Motivation for a differentiable inversion method

The approach developed in this work treats the PV operator

$$\mathcal{K}[H^{(+)}](\xi, t, Q^2) \equiv \Re e \mathcal{H}(\xi, t, Q^2)$$

as a known, fixed, differentiable operator that is embedded directly inside a neural network. The network outputs $H^{(+)}(x, \xi, t, Q^2)$ on a discretized x -grid, while the PV kernel acts as a fixed layer that produces $\Re e \mathcal{H}$ during training. This structure offers several advantages:

- it enforces exact C-parity and endpoint suppression;
- it preserves the analytic structure of QCD factorization;
- it enables gradient-based training directly on $\Re e \mathcal{H}$;
- it provides a natural way to implement regularization in the GPD domain, such as curvature penalization in x , ξ , and t ;
- it allows uncertainty quantification via the method of Monte-Carlo (replica) ensembles, yielding a probabilistic extraction of the full GPD.

This section sets the mathematical stage for the differentiable inversion pipeline developed in Sec. III, where we specify the PV operator, the neural-network architecture, the smoothness priors, and the replica ensemble used to propagate experimental uncertainties into the extracted GPD.

III. DIFFERENTIABLE PV INVERSION AND NEURAL-NETWORK FRAMEWORK

In this section we introduce the differentiable operator that implements the principal-value (PV) convolution integral transform defining $\Re e \mathcal{H}$. We also describe the neural-network architecture used to represent the underlying charge-weighted GPD $H^{(+)}(x, \xi, t, Q^2)$. The key idea is to embed all analytic QCD structure-symmetry under $x \rightarrow -x$, endpoint behavior, and the PV Hilbert-type

kernel-directly into the model so that training occurs in the GPD space while the predicted CFF is obtained by exact PV integral transform inside the computational graph (directed network of tensor operations built during the forward pass).

A. Discretized principal-value operator

At leading order, the real part of the CFF is related to the C -even GPD by the singular PV convolution

$$\Re e \mathcal{H}(\xi, t, Q^2) \stackrel{\text{LO}}{=} \text{PV} \int_0^1 dx \left[\frac{1}{\xi - x} - \frac{1}{\xi + x} \right] H^{(+)}(x, \xi, t, Q^2), \quad (7)$$

cf. Eq. (5). For the numerical implementation we evaluate this integral on a fixed x -grid. Let $\{x_i\}_{i=1}^{N_x}$ be a uniform grid on $[-1, 1]$ with spacing $\Delta x = x_{i+1} - x_i$, and define symmetric trapezoidal weights

$$w_1 = w_{N_x} = \frac{\Delta x}{2}, \quad w_i = \Delta x \quad (2 \leq i \leq N_x - 1). \quad (8)$$

Using the C -even property

$$H^{(+)}(-x, \xi, t, Q^2) = -H^{(+)}(x, \xi, t, Q^2), \quad (9)$$

we can write the discretized PV operator as

$$\Re e \mathcal{H}(\xi, t, Q^2) = \sum_{i=1}^{N_x} w_i K_i(\xi) H^{(+)}(x_i, \xi, t, Q^2), \quad (10)$$

with kernel

$$K_i(\xi) = \left[\frac{1}{\xi - x_i} - \frac{1}{\xi + x_i} \right] \Theta(|x_i - \xi| - \varepsilon_{\text{PV}}), \quad (11)$$

where $\Theta(u)$ denotes the Heaviside step function, $\Theta(u) = 1$ for $u \geq 0$ and $\Theta(u) = 0$ otherwise, and ε_{PV} defines the excluded region around $x = \xi$ used to implement the principal value numerically. In practice we choose $\varepsilon_{\text{PV}} = n_{\text{PV}} \Delta x$ with $n_{\text{PV}} \simeq 2-3$, which provides a stable approximation to the PV integral while avoiding contamination from the singular point $x = \xi$.

The discrete operator (Eq. (10)) is implemented as a tensorized map (i.e., differentiable map acting on batched tensors) inside PyTorch, so that its gradients with respect to $H^{(+)}(x_i, \xi, t, Q^2)$ are obtained automatically by backpropagation. This makes the full inverse problem differentiable and suitable for gradient-based optimization.

B. Neural-network representation of $H^{(+)}$

We represent the GPD $H^{(+)}$ by a feed-forward neural network augmented with analytic factors that impose the known symmetries:

$$H_{\theta}^{(+)}(x, \xi, t, Q^2) = E(x) O[f_{\theta}](x, \xi, t, Q^2), \quad (12)$$

where f_{θ} is a basic deep neural network (DNN) with trainable parameters θ , and the two multiplicative operators enforce:

1. *Exact oddness in x :*

$$O[f_{\theta}](x, \xi, t, Q^2) = \frac{1}{2} \left[f_{\theta}(x, \xi, t, Q^2) - f_{\theta}(-x, \xi, t, Q^2) \right], \quad (13)$$

so that $H_{\theta}^{(+)}(-x, \xi, t, Q^2) = -H_{\theta}^{(+)}(x, \xi, t, Q^2)$ by construction.

2. *Endpoint suppression:*

$$E(x) = (1 - |x|)^{\beta}, \quad \beta > 0, \quad (14)$$

ensuring that $H_{\theta}^{(+)} \rightarrow 0$ as $|x| \rightarrow 1$.

The input variables are normalized according to

$$\tilde{\xi} = \frac{\xi - \mu_{\xi}}{\sigma_{\xi}}, \quad \tilde{t} = \frac{t - \mu_t}{\sigma_t}, \quad \tilde{q}^2 = \frac{\ln Q^2 - \ln \mu_{Q^2}}{\sigma_{Q^2}}, \quad (15)$$

and the DNN receives the four-dimensional feature vector $(x, \tilde{\xi}, \tilde{t}, \tilde{q}^2)$ as input. In the present analysis we take f_{θ} to be a two-layer DNN with $N_h = 64$ hidden units per layer and tanh activations, which provides a sufficiently expressive yet stable representation for the inverse problem. Training is performed using the Adam optimizer with learning rate $\eta_0 = 2 \times 10^{-2}$.

C. Smoothness priors and regularization

Because the mapping $H^{(+)} \mapsto \Re e \mathcal{H}$ is a singular integral transform, the inverse problem amplifies high-frequency oscillations in x , ξ , and t . To stabilize the reconstruction we introduce smoothness priors directly in the GPD domain, in addition to using a smooth, global representation of the input CFFs:

Curvature regularization in x : We penalize the squared second derivative of $H_{\theta}^{(+)}$ with respect to x ,

$$R_x = \lambda_x \int_0^1 dx \left[\frac{\partial^2 H_{\theta}^{(+)}}{\partial x^2} \right]^2, \quad (16)$$

whose discretized form uses the standard finite difference

$$\frac{\partial^2 H^{(+)}(x_i)}{\partial x^2} \simeq \frac{H^{(+)}(x_{i+1}) - 2H^{(+)}(x_i) + H^{(+)}(x_{i-1})}{\Delta x^2}.$$

This term suppresses unphysical oscillations in the x -shape that would otherwise be amplified by the PV kernel.

Kinematic smoothness in ξ and t : Where data coverage allows, we optionally include analogous terms

$$R_{\xi} = \lambda_{\xi} \int_0^1 dx \left[\frac{\partial^2 H_{\theta}^{(+)}}{\partial \xi^2} \right]^2, \quad (17)$$

$$R_t = \lambda_t \int_0^1 dx \left[\frac{\partial^2 H_{\theta}^{(+)}}{\partial t^2} \right]^2, \quad (18)$$

approximated by second differences in ξ and t at fixed x . These priors suppress rapid kinematic fluctuations that are not supported by the experimental CFF uncertainties. In the numerical studies presented below, we primarily use the x -curvature prior R_x and treat R_ξ and R_t as optional stabilizers; setting $\lambda_\xi = \lambda_t = 0$ recovers an inversion regularized purely in x .

Loss function: Given an input set of kinematic points $\{(\xi_n, t_n, Q_n^2)\}$ and corresponding CFF values $\Re \mathcal{H}_n^{(\text{exp})}$ with uncertainties σ_n , the scalar loss minimized during training is

$$\mathcal{L} = \sum_n \frac{[\Re \mathcal{H}_\theta(\xi_n, t_n, Q_n^2) - \Re \mathcal{H}_n^{(\text{exp})}]^2}{\sigma_n^2} + R_x + R_\xi + R_t, \quad (19)$$

where $\Re \mathcal{H}_\theta$ is obtained from $H_\theta^{(+)}$ via the discrete PV operator (Eq. (10)). All terms are implemented as differentiable PyTorch operations and evaluated in vectorized form.

D. Replica ensemble and uncertainty propagation

To propagate experimental uncertainties into the extracted GPD, we adopt a Monte-Carlo replica strategy, similar to global CFF [51] and TMD analyses [52, 53]. For each replica r we generate a synthetic CFF dataset

$$\Re \mathcal{H}_n^{(r)} = \Re \mathcal{H}_n^{(\text{exp})} + \sigma_n \delta_n^{(r)}, \quad \delta_n^{(r)} \sim \mathcal{N}(0, 1), \quad (20)$$

and train an independent copy of the network to minimize (19). The resulting set of functions $\{H_{\theta_r}^{(+)}(x, \xi, t, Q^2)\}_{r=1}^{N_{\text{rep}}}$ provides a nonparametric Monte-Carlo representation of the posterior distribution over the GPD. Ensemble means and standard deviations are then computed pointwise in (x, ξ, t, Q^2) , yielding credible intervals and correlation information at any desired kinematic point.

Because both the PV operator and the smoothness priors are implemented as differentiable PyTorch layers, the full mapping

$$(\xi, t, Q^2) \longrightarrow H^{(+)}(x, \xi, t, Q^2)$$

is trained end-to-end without external approximations. The replica ensemble therefore represents a model-independent inversion of the input CFF data into the underlying GPD, with uncertainties reflecting the propagated experimental covariance together with the controlled smoothness assumptions encoded in R_x , R_ξ , and R_t .

IV. IMPLEMENTATION AND NUMERICAL WORKFLOW

This section summarizes the computational method used to implement the differentiable PV inversion, train

the neural-network representation of the GPD, and propagate experimental uncertainties through a replica ensemble. The full pipeline is end-to-end differentiable and implemented in PyTorch [42], allowing gradients to flow from the CFF loss function (Eq. (19)) back through the principal-value convolution to the GPD itself.

A. Numerical x -grid and PV mask

All numerical evaluations of the GPD and of the PV operator employ the discretization introduced in Sec. II, Eqs. (8)–(11). For completeness we summarize here the specific choices used in the implementation.

The GPD is represented on a uniform grid

$$x_i \in [-1, 1], \quad i = 1, \dots, N_x, \quad \Delta x = \frac{2}{N_x - 1}, \quad (21)$$

with $N_x = 181$ points. This uniform grid simplifies both the evaluation of the PV kernel and the finite-difference estimates of the curvature penalty discussed below.

The quadrature weights entering the discrete PV operator (Eq. (10)) are taken to be those of the trapezoidal rule,

$$w_1 = w_{N_x} = \frac{\Delta x}{2}, \quad w_i = \Delta x \quad (2 \leq i \leq N_x - 1), \quad (22)$$

which is sufficient given the smoothness of $H^{(+)}(x, \xi, t, Q^2)$ enforced by the regularization.

The principal-value singularity at $x = \pm \xi$ is treated by excising a small region around these points in the discrete sum, as in Eq. (11). In practice we set

$$\varepsilon_{\text{PV}} = n_{\text{PV}} \Delta x, \quad n_{\text{PV}} \simeq 2-3, \quad (23)$$

so that all grid points satisfying $|x_i - \xi| < \varepsilon_{\text{PV}}$ or $|x_i + \xi| < \varepsilon_{\text{PV}}$ are omitted from the integration. We have verified that moderate variations of (N_x, n_{PV}) in these ranges do not change the extracted GPD within the quoted uncertainty bands, but values outside this window either under-resolve the x dependence or reintroduce numerical instabilities in the PV integral.

B. Treatment of the PV singularity

The singularity at $x = \xi$ in Eq. (7) is handled by excluding a symmetric region

$$|x_i - \xi| \leq \varepsilon_{\text{PV}}, \quad \varepsilon_{\text{PV}} = n_{\text{PV}} \Delta x, \quad (24)$$

with $n_{\text{PV}} = 2-3$. This effectively implements a numerical principal value. We explicitly verified that the inversion is stable against moderate variations in the cutoff size, and all results reported in this work correspond to $n_{\text{PV}} = 2$.

The PV mask is applied to the kernel at the tensor level, so that the gradient of the masked kernel with respect to $H^{(+)}(x_i)$ is exactly zero inside the excised region. This suppresses numerical instabilities associated with the divergent kernel and eliminates the need for explicit analytic symmetrization.

C. Differentiable PV operator

The forward mapping

$$(\xi, t, Q^2) \mapsto \Re e \mathcal{H}_\theta(\xi, t, Q^2)$$

is implemented as a PyTorch function: Given index sets for the PV mask $\mathcal{M}(\xi)$, the convolution is evaluated as

$$\Re e \mathcal{H}_\theta(\xi, t, Q^2) = \sum_{i \in \mathcal{M}(\xi)} w_i \left[\frac{1}{\xi - x_i} - \frac{1}{\xi + x_i} \right] H_\theta^{(+)}(x_i, \xi, t, Q^2). \quad (25)$$

Because all operations are PyTorch primitives, backpropagation passes exactly through the PV integrand, the

envelope factor, the oddness projection, and the DNN, enabling efficient gradient-based inversion.

D. Smoothness priors

To ensure numerical stability and physical plausibility, we impose the regularization terms discussed in Sec. III C.

(i) *Curvature in x :* We compute the curvature energy

$$\mathcal{R}_x = \lambda_x \sum_{i=2}^{N_x-1} \left[\frac{H_\theta^{(+)}(x_{i+1}) - 2H_\theta^{(+)}(x_i) + H_\theta^{(+)}(x_{i-1})}{\Delta x^2} \right]^2 \Delta x, \quad (26)$$

where typical values are $\lambda_x = (1\text{-}5) \times 10^{-3}$.

(ii) *Smoothness in ξ and t :* At training points (ξ_n, t_n) , we evaluate second finite differences in the kinematic variables:

$$\mathcal{R}_\xi = \lambda_\xi \sum_i \left[\frac{H_\theta^{(+)}(x_i, \xi + \delta\xi, t) - 2H_\theta^{(+)}(x_i, \xi, t) + H_\theta^{(+)}(x_i, \xi - \delta\xi, t)}{\delta\xi^2} \right]^2 \Delta x, \quad (27)$$

$$\mathcal{R}_t = \lambda_t \sum_i \left[\frac{H_\theta^{(+)}(x_i, \xi, t + \delta t) - 2H_\theta^{(+)}(x_i, \xi, t) + H_\theta^{(+)}(x_i, \xi, t - \delta t)}{\delta t^2} \right]^2 \Delta x. \quad (28)$$

We use $\delta\xi \simeq 0.02$ and $\delta t \simeq 0.10 \text{ GeV}^2$, and choose (λ_ξ, λ_t) in the range $(0.5\text{-}2) \times 10^{-3}$.

The scalar loss minimized during training is

$$\mathcal{L} = \sum_n \frac{[\Re e \mathcal{H}_\theta(\xi_n, t_n, Q_n^2) - \Re e \mathcal{H}_n^{(\text{exp})}]^2}{\sigma_n^2} + \mathcal{R}_x + \mathcal{R}_\xi + \mathcal{R}_t. \quad (29)$$

All terms are differentiable and efficiently computed in vectorized form.

E. Replica ensemble training

Experimental uncertainty quantification is achieved via a Monte-Carlo ensemble

$$\Re e \mathcal{H}_n^{(r)} = \Re e \mathcal{H}_n^{(\text{exp})} + \sigma_n \delta_n^{(r)}, \quad \delta_n^{(r)} \sim \mathcal{N}(0, 1), \quad (30)$$

with $r = 1, \dots, N_{\text{rep}}$ replicas.

Each replica trains an independent network with freshly drawn CFF within the sample space defined by the scale of the experimental error determined by the global CFF model [40]. The resulting set of GPDs

$$\{H_{\theta_r}^{(+)}(x, \xi, t, Q^2)\}_{r=1}^{N_{\text{rep}}}$$

represents an empirical posterior distribution. Ensemble means and standard deviations are computed pointwise,

providing credible intervals for $H^{(+)}$ across the entire (x, ξ, t, Q^2) domain.

Training typically converges within $\sim 50\text{-}150$ epochs for each replica, depending on the regularization strength. Replica jobs are trivially parallelizable on multi-GPU systems.

V. GPD CLOSURE TEST

Before applying the inversion to experimental CFFs, we perform a closure test in which both the *data* and the target GPD are known analytically. This allows us to quantify the intrinsic methodological error of the PV-DNN inversion and to tune the curvature regularization strength λ_x that appears in Sec. IV.

A. Analytic truth model and synthetic CFFs

For the test we specify a smooth, odd GPD

$$H_{\text{fit}}^{(+)}(x, \xi, t, Q^2) = A(\xi, t, Q^2) f(x) E(x), \quad (31)$$

$$f(x) = x(1-x^2)^2, \quad (32)$$

$$E(x) = (1-|x|)^2, \quad (33)$$

$$A(\xi, t, Q^2) = \sum_{\substack{i,j,k \geq 0 \\ i+j+k \leq 2}} a_{ijk} U(\xi)^i V(t)^j W(Q^2)^k, \quad (34)$$

$$U(\xi) = 2\xi - \frac{1}{2}, \quad V(t) = \frac{t}{1 \text{ GeV}^2} + \frac{1}{2}, \quad (35)$$

$$W(Q^2) = \ln\left(\frac{Q^2}{Q_*^2}\right).$$

To parameterize this function to use as the closure test generator we first perform an initial GPD extraction on the CFF mean, and then perform a fit to the GPD to obtain $H_{\text{true}}^{(+)}(x, \xi, t, Q^2)$ on $x \in [-1, 1]$.

The corresponding *true* CFF $\Re e \mathcal{H}_{\text{true}}$ is obtained by applying exactly the same discrete PV operator as used in the network architecture. On the x -grid $\{x_n\}_{n=1}^{N_x}$ with quadrature weights $\{w_n\}$,

$$\Re e \mathcal{H}_{\text{true}}(\xi, t, Q^2) = \frac{1}{2} \sum_{n=1}^{N_x} H_{\text{true}}^{(+)}(x_n, \xi, t, Q^2) K_n(\xi) w_n, \quad (36)$$

where the discrete kernel

$$K_n(\xi) = \left[\frac{1}{\xi - x_n} - \frac{1}{\xi + x_n} \right] \Theta(|x_n - \xi| > \varepsilon_{\text{PV}}) \Theta(|x_n + \xi| > \varepsilon_{\text{PV}}) \quad (37)$$

implements the numerical principal value with an exclusion half-width $\varepsilon_{\text{PV}} = n_{\text{PV}} \Delta x$, as in Eq. (11). The synthetic dataset is built by evaluating Eq. (36) on the same (ξ, t, Q^2) grid used later in the analysis. In the baseline closure test we set the noise to zero, so that any discrepancy between the reconstructed GPD and $H_{\text{true}}^{(+)}$ is purely algorithmic. The goal is then to ensure this contribution to algorithmic error is minimized over phase space.

B. Curvature regularization as Tikhonov stabilization

Training the PV-DNN on this synthetic dataset corresponds, in the continuum, to minimizing a regularized functional of the form

$$\mathcal{J}[H^{(+)}] = \chi^2 [\Re e \mathcal{H}[H^{(+)}]] + \lambda_x R_x[H^{(+)}, \quad (38)$$

where χ^2 measures the misfit between the PV projection of the network GPD and the pseudo-data, and

$$R_x[H^{(+)}] = \int_{-1}^1 dx (\partial_x^2 H^{(+)}(x, \xi, t, Q^2))^2 \quad (39)$$

is a second-order Tikhonov penalty in x [9, 50]. In the discrete implementation λ_x multiplies exactly this term: the network computes $H^{(+)}(x_n)$ on the fixed x grid, the second derivative is approximated by the centered finite difference $H_{n+1}^{(+)} - 2H_n^{(+)} + H_{n-1}^{(+)}$, and R_x is obtained by summing the squared curvature over n with the appropriate factor of Δx . Thus λ_x controls the trade-off between fitting $\Re e \mathcal{H}$ and enforcing smoothness in x .

Upon discretization of the x -integral on a fixed grid $\{x_i\}$ and evaluation of the CFF on a set of kinematic points $\{(\xi_j, t_j, Q_j^2)\}$, the principal-value operator defines a linear map between the discretized GPD and CFF,

$$y_j \equiv \Re e \mathcal{H}(\xi_j, t_j, Q_j^2) = \sum_{i=1}^{N_x} w_i K_{ji} h_i, \quad (40)$$

where $h_i \equiv H^{(+)}(x_i, \xi_j, t_j, Q_j^2)$ and the kernel matrix K_{ji} is given by Eq. (11). In matrix notation this relation reads $\mathbf{y} = \mathbf{K} \mathbf{h}$.

From the point of view of inverse problems, Eq. (38) is a standard second-order Tikhonov regularization [9] of the Fredholm equation (Eq. (5)). If one discretizes the PV integral as $\mathbf{y} = \mathbf{K} \mathbf{h}$, where \mathbf{y} collects $\Re e \mathcal{H}$ on the (ξ, t, Q^2) grid and \mathbf{h} collects $H^{(+)}$ on the x grid, then minimizing Eq. (38) is equivalent to solving the modified normal equations

$$(\mathbf{K}^T \mathbf{W} \mathbf{K} + \lambda_x \mathbf{L}^T \mathbf{L}) \mathbf{h} = \mathbf{K}^T \mathbf{W} \mathbf{y}, \quad (41)$$

with \mathbf{W} the inverse covariance of the CFF pseudo-data and \mathbf{L} the discrete second-derivative operator. The PV kernel has rapidly decaying singular values, so the unregularized system ($\lambda_x = 0$) amplifies high-frequency components of \mathbf{y} , making the inversion highly sensitive to numerical noise or to small inconsistencies in the data. The term $\lambda_x \mathbf{L}^T \mathbf{L}$ suppresses precisely those high-curvature modes of \mathbf{h} , rendering the problem numerically well conditioned at the price of a controlled bias toward smoother solutions.

C. The Tuning Process

To ensure that the tuning procedure is not limited by sampling artifacts, the CFF pseudo-data used in closure tests should densely cover the phase space of interest. This reflects the situation in an experimental extraction, where the inversion begins from a smooth, continuous CFF representation—most naturally provided by a global DNN fit to the measured cross sections and asymmetries. Preliminary studies are therefore used to determine an x - and (ξ, t, Q^2) -grid that is fine enough to avoid discretization-induced error while remaining computationally tractable.

The first step in the tuning process is to perform single-sample trials to verify that the linear PV integral transform can reproduce the analytic test GPD with essentially machine precision across the kinematic domain. After this baseline is established, a large set (e.g., 200) of identical

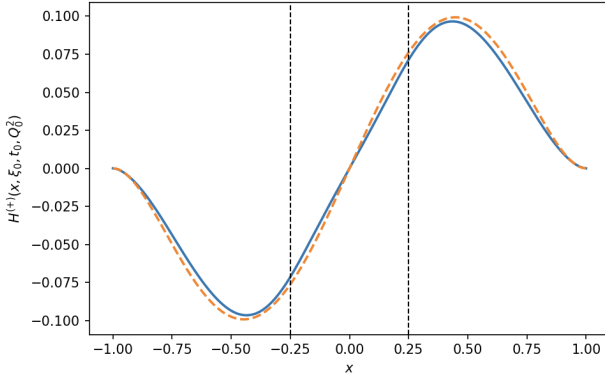


FIG. 1. Reconstructed one-dimensional slice of $H^{(+)}(x | \xi_0, t_0, Q_0^2)$ at the median kinematic point of the data, corresponding to $\xi_0 = 0.25$, $t_0 = -0.750 \text{ GeV}^2$, and $Q_0^2 = 3.75 \text{ GeV}^2$ showing a comparison between the true analytic function and the reconstructed GPD. The solid line represents the 1 replica instance and the dashed line represent the true function.

replicas is run without adding simulated experimental noise. These noiseless replicas isolate the intrinsic algorithmic error of the inversion—i.e., the error associated solely with numerical discretization, network capacity, and the PV kernel. Hyperparameters are then adjusted until this algorithmic error becomes negligible compared with the uncertainties expected from realistic CFF inputs.

In practice, we do not form Eq. (41) explicitly; instead, the PV operator is implemented as a differentiable layer and Eq. (38) is minimized by gradient descent. The variation in λ_x in the closure test is a critical first phase of tuning. For very small λ_x , the network reproduces $\Re\mathcal{H}_{\text{true}}$ essentially perfectly, but the reconstructed $H^{(+)}$ can develop unphysical wiggles in x that are invisible to the PV projection. For very large λ_x the curvature penalty dominates, driving $H^{(+)}$ toward a function with nearly vanishing second derivative (approximately linear in x), and the fit to $\Re\mathcal{H}_{\text{true}}$ deteriorates.

Between these extremes there is an intermediate window of λ_x for which both the projected CFFs and the underlying GPD are well reproduced. In this regime the curvature penalty damps only those modes that are poorly constrained by the PV kernel, while leaving the large-scale structure of $H^{(+)}$ essentially unchanged. The value of λ_x used in the main analysis is chosen in this window, by requiring that $\Re\mathcal{H}_{\text{true}}$ be fitted within numerical precision and that the root-mean squared (RMS) deviation between the reconstructed $H^{(+)}$ and the analytic $H_{\text{true}}^{(+)}$ remain small compared to the natural scale of the GPD.

Figure 1 shows a representative closure test at (ξ_0, t_0, Q_0^2) , comparing $H_{\text{true}}^{(+)}(x, \xi_0, t_0, Q_0^2)$ (dashed line) with the GPD reconstructed by the PV-DNN at the tuned λ_x (solid line). The two curves are close over most of x , with residual differences on the order of 10^{-6} , and the largest part of the amplitude is 0.1. This residual can be interpreted as a methodological error of the inversion for noise-free CFFs. In a realistic application, where exper-

imental errors and limited kinematic coverage enter via the replica ensemble, the closure error provides a lower bound on the achievable precision of the GPD. Regions of phase space with dense, precise CFF information are effectively well conditioned and yield narrow GPD bands, while in sparse or noisy regions the ill-posed PV kernel unavoidably amplifies experimental uncertainties, leading to broader, but still smooth, uncertainty bands in $H^{(+)}$.

In addition to the curvature weight λ_x and the overall network capacity, a small set of hyperparameters largely controls the inversion behavior. The number of x grid points N_x and the principal-value mask n_{PV} (entering $\varepsilon_{\text{PV}} = n_{\text{PV}} \Delta x$) determine how finely the GPD is resolved and how aggressively the singular region near $x = \pm \xi$ is excluded. Larger N_x improves resolution but makes the PV operator more ill-conditioned, while smaller n_{PV} uses more of the data but increases sensitivity to numerical noise. The exponent β in the factor $(1 - |x|)^\beta$ controls how strongly the GPD is suppressed as $|x| \rightarrow 1$. This acts as a built-in prior to endpoint behavior: larger β enforces faster fall-off and reduces sensitivity to poorly constrained regions near $|x| = 1$, while smaller β allows for more structure there.

The DNN complexity, defined by the number of nodes per hidden layer—the network’s width—and the number of hidden layers—the network’s depth—are tuned, and the learning rate, batch size, and number of epochs control how closely the network can approach the minimum of the regularized loss. Insufficient training (or too large a learning rate) leaves a noticeable mismatch between predicted and synthetic CFFs even in closure tests, while overtraining at very small λ_x can re-introduce oscillatory modes despite the curvature term.

Taken together, these parameters control the balance between fidelity to the input CFFs and smoothness of the reconstructed GPD. To quantify the resulting *methodological* error across phase space, we carry out a sequence of dedicated closure tests in which synthetic CFFs are generated from a known analytic test function $H_{\text{true}}^{(+)}$ and passed through the full PV-DNN inversion. The reconstruction fidelity is examined as a function of the hyperparameter configuration and under controlled variations of the analytic test function, with the scan restricted to the physically relevant domain suggested by the global CFF model extracted from data.

This calibration requires an iterative procedure [51, 52]. An initial DNN fit to the experimental CFFs provides a smooth mean CFF representation, from which a preliminary GPD model is obtained using the PV-DNN inversion with algorithmic error only. This preliminary GPD is then *fitted* using the smooth analytic functional form of Eq. (31), thereby producing an analytic surrogate $H_{\text{true}}^{(+)}$ that is both physically realistic and consistent with the experimentally constrained CFF behavior. Closure tests performed with this analytic surrogate allow the closure error to be mapped out across the hyperparameter space $(\lambda_x, N_x, n_{\text{PV}}, L, H)$, and the procedure is repeated until a stable region of hyperparameters is identified.

Although the present study varies only the curvature weight λ_x , in principle the analogous smoothness parameters λ_ξ and λ_t , which control regularization in the skewness and momentum-transfer directions, may also be tuned in the same manner. In the present work we employ only the x -curvature regularization $\lambda_x R_x$, since the ill-posedness of the PV inversion arises primarily from the projection along the internal momentum fraction x . The external kinematic dependence in (ξ, t, Q^2) is already encoded smoothly in the global CFF DNN fit used as input, so additional curvature penalties in ξ and t would risk over-regularizing the solution and obscuring genuine structure.

After this calibration phase, the hyperparameters are fixed in a two-step strategy: they are first tuned using the analytic closure tests, where the bias with respect to $H_{\text{true}}^{(+)}$ can be measured directly, and the same settings are subsequently applied to the real CFF ensemble so that the propagated GPD uncertainties reflect experimental errors rather than limitations of the inversion machinery.

VI. GPD EXTRACTION

In this section we present the results of the GPD extraction obtained from the differentiable PV inversion previously described. The analysis is based on the DNN model of the CFF determined from experimental DVCS data and their propagated uncertainties, which enter as input to the inversion together with the N_{rep} -member replica ensemble used to propagate experimental errors into the extracted GPD. All GPD quantities shown below correspond to the C-even quark combination $H^{(+)}(x, \xi, t, Q^2)$ evaluated on the fixed x -grid employed during training.

A. One-dimensional GPD slices

A convenient way to visualize the reconstruction is to evaluate the GPD on a fixed (ξ_0, t_0, Q_0^2) slice and display the x -dependence together with its pointwise uncertainty. Figure 2 shows the ensemble-averaged $H^{(+)}(x)$ for the median kinematic point of the dataset,

$$(\xi_0, t_0, Q_0^2) = (\text{median}(\xi), \text{median}(t), \text{median}(Q^2)).$$

The solid curve denotes the ensemble mean and the shaded band indicates the 1σ uncertainty inferred from the replica variance.

Several features are immediately visible: (i) the exact oddness in x enforced by the architecture, (ii) the suppression near $|x| \rightarrow 1$ due to the endpoint envelope, and (iii) a smooth behavior near $x = \xi_0$, where the PV kernel is most sensitive. Importantly, the uncertainty band naturally widens deep in the ERBL region and at large $|x|$, consistent with the reduced constraining power of the experimental CFFs in those domains.

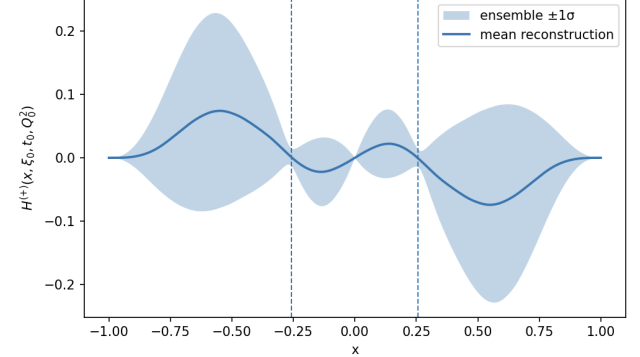


FIG. 2. Reconstructed one-dimensional slice of $H^{(+)}(x | \xi_0, t_0, Q_0^2)$ at the median kinematic point of the data, corresponding to $\xi_0 = 0.257$, $t_0 = -0.742 \text{ GeV}^2$, and $Q_0^2 = 4.81 \text{ GeV}^2$. The solid line represents the ensemble mean and the shaded region the 68% credible band obtained from the replica distribution. The vertical dashed lines mark $x = \pm \xi_0$.

B. Three-dimensional GPD surfaces

To illustrate the full multidimensional structure, we evaluate $H^{(+)}(x_0, \xi, t, Q_0^2)$ for a fixed value of x_0 and map its dependence on the two experimentally accessible variables (ξ, t) . Figure 3 shows the resulting three-dimensional surface at

$$x_0 = 0.257, \quad Q_0^2 = 4.81 \text{ GeV}^2.$$

The plotted surface corresponds to the ensemble mean over N_{rep} trained replicas, with translucent sheets indicating the $\pm 1\sigma$ envelope. This visualization reveals the nontrivial evolution of the amplitude across both the DGLAP region ($\xi < x_0$) and the ERBL region ($\xi > x_0$). The shape along t is driven primarily by the data coverage and the smoothness priors, while the ridge-like behavior near $\xi = x_0$ reflects the kinematic location where the CFF kernel is maximally sensitive.

C. Scale dependence of the reconstructed GPD

An advantage of the neural representation is that the Q^2 degree of freedom enters the network on equal footing with (x, ξ, t) , enabling evaluation of the reconstructed GPD at arbitrary virtualities within the kinematic support of the input CFF ensemble. Although the training data span only a limited set of Q^2 values, the network learns a smooth interpolation driven by the $\ln Q^2$ normalization in the input layer and the regularity of the learned GPD.

To illustrate this, Fig. 4 shows three GPD surfaces, all at fixed x_0 , but for $Q_0^2 = \{1, 4, 8\} \text{ GeV}^2$. The surfaces are plotted together on common (ξ, t) axis vs $H^{(+)}(x_0, \xi, t, Q_0^2)$ with partial transparency. The variation across scales is smooth, consistent with the slowly varying scale dependence in the measured CFFs. The method makes no assumption of perturbative GPD evolution; rather, the

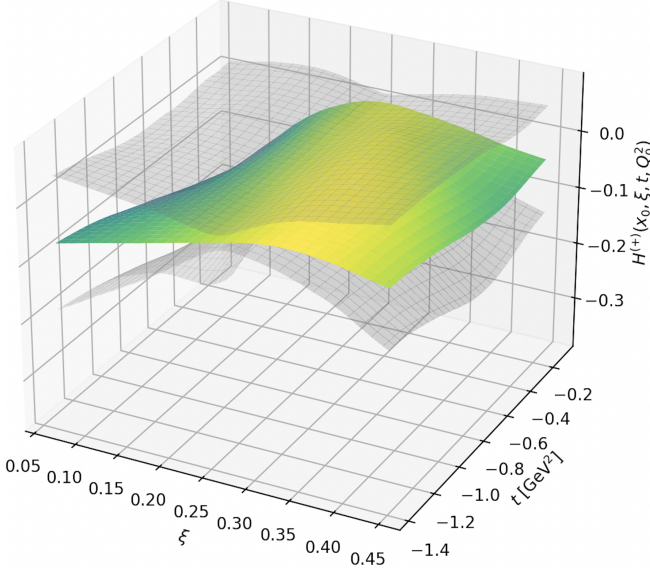


FIG. 3. Three-dimensional GPD surface $H^{(+)}(x_0, \xi, t, Q_0^2)$ evaluated at fixed $x_0 = 0.257$ and $Q_0^2 = 4.81 \text{ GeV}^2$. The colored sheet shows the ensemble mean over N_{rep} replicas, while the two translucent sheets above and below indicate the $\pm 1\sigma$ uncertainty band. The plane $\xi = x_0$ separates the DGLAP ($\xi < x_0$) and ERBL ($\xi > x_0$) domains.

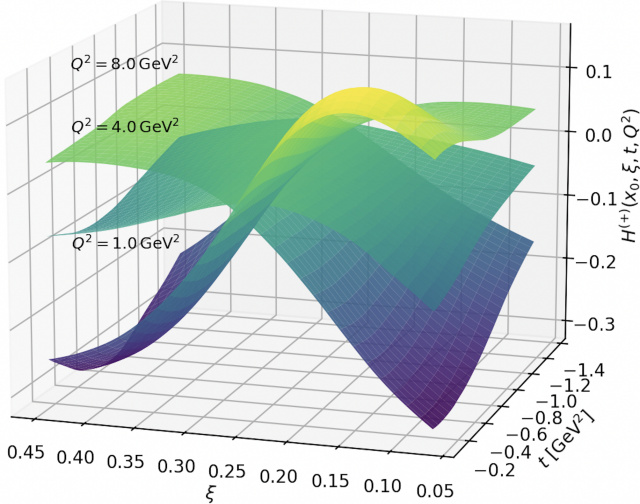


FIG. 4. Comparison of reconstructed surfaces $H^{(+)}(x_0, \xi, t, Q_0^2)$ at fixed $x_0 = 0.257$ and three values of the virtuality, $Q_0^2 = 1, 4, 8 \text{ GeV}^2$. All surfaces are ensemble means plotted on the same (ξ, t, z) axes. Differences across the three scales reflect the smooth Q^2 dependence inferred from the experimental CFFs and the learned representation. No uncertainty bands are shown for clarity.

dependence in Q^2 emerges entirely from the experimental inputs and the regularities imposed by the inversion architecture. We note the reversed trend for the lower Q^2 surface as seen for the higher Q^2 surface along ξ . No errors are shown so the contrasting trends are more visible.

D. Stability and uncertainty

The replica ensemble produces a full probability distribution for the GPD at each (x, ξ, t, Q^2) . The resulting credible intervals (Fig. 2) and the stability of the three-dimensional surfaces (Figs. 3, 4) provide strong evidence that the differentiable PV inversion is robust against the experimental noise in the input CFFs and against moderate variations of the PV mask and regularization strengths. In particular, the curvature-based priors prevent the oscillatory artifacts that typically plague direct inversions of Eq. (7), while preserving genuine structure dictated by the data.

VII. DISCUSSION AND OUTLOOK

The approach presented here demonstrates that the inverse problem linking the real part of the DVCS Compton form factor $\Re e \mathcal{H}$ to the underlying GPD $H^{(+)}(x, \xi, t, Q^2)$ can be solved in a stable and data-driven manner using differentiable physics layers embedded within a neural-network architecture. By enforcing exact structural constraints—oddness in x , endpoint behavior, and the analytic form of the PV convolution kernel—the method avoids the model-dependent assumptions that traditionally enter GPD parametrizations. The representation learns the GPD directly from experimental information, regularized only by smoothness priors motivated by the mathematical structure of the inverse problem.

The replica ensemble plays a dual role. First, it propagates the experimental uncertainties, including their full correlations, into a probabilistic description of the GPD. Second, it provides a valuable diagnostic of inversion stability. The consistent behavior of the ensembles across (x, ξ, t, Q^2) —particularly the widening of the uncertainty band in the ERBL region and at large $|x|$ —is fully compatible with the kinematic sensitivity of the PV kernel and the coverage of the experimental CFF data. Importantly, the reconstructed three-dimensional GPD surfaces show smooth and physically reasonable trends without exhibiting artificial oscillations, highlighting the effectiveness of the curvature priors in suppressing modes amplified by the PV operator.

A. Connection to DVCS phenomenology

From a phenomenological perspective, this approach provides a model-independent alternative to double-distribution ansätze, Regge-inspired parametrizations, and truncated polynomial expansions. Because the GPD is learned directly in the kinematic variables (x, ξ, t, Q^2) , the method naturally accommodates:

- the separation between DGLAP and ERBL domains,

- the ridge-like sensitivity near $x = \xi$ imposed by the PV kernel,
- the gradual Q^2 dependence reflected in the experimental CFF dataset,
- the strongly t -dependent falloff determined by the data.

Although no dynamical QCD evolution equations are imposed, the learned Q^2 dependence is found to be smooth and well-behaved, reflecting both the kinematic normalization in the input layer and the weak Q^2 variation of the CFFs in the fitted region. In future work, the network structure could be extended to incorporate leading-order or next-to-leading-order (NLO) QCD evolution [7] as a differentiable layer, enabling comparative scale evolution studies directly from data.

B. Toward global GPD extraction

The present study focuses on the inversion of $\Re e \mathcal{H}$, but the approach generalizes immediately to the other quark and gluon CFFs \mathcal{E} , $\tilde{\mathcal{H}}$, and $\tilde{\mathcal{E}}$. A full global analysis would combine:

1. Unpolarized cross sections, beam-spin and beam-charge asymmetries, target-spin (longitudinal and transverse) asymmetries, and double-spin asymmetries, together with polarized and longitudinally separated cross sections.
2. Next-generation CFF extractions that use DNNs to build global models with low uncertainty across phase space.
3. Future high-precision measurements with multiple observables taken simultaneously.
4. Access to raw, unbinned data for optimal sampling of experimental features and covariances.

An important practical extension of the present method is to treat the real and imaginary parts of a given CFF on the same footing. At leading order, the imaginary part of \mathcal{H} fixes $H^{(+)}$ on the cross-over line $x = \xi$, while the real part is obtained from the PV integral of Eq. (5). Embedding both kernels as differentiable layers in a single network would allow one to train simultaneously on $\Re e \mathcal{H}$ and $\Im m \mathcal{H}$ data, so that the learned GPD is constrained both by its bulk x -dependence and by its value on the cross-over line. In such a setup, dispersion relations between $\Re e \mathcal{H}$ and $\Im m \mathcal{H}$ can be implemented as an internal consistency condition or soft penalty, turning the full complex CFF into a stringent, data-driven constraint on the same underlying $H^{(+)}$. This joint use of real and imaginary parts is expected to reduce degeneracies in the inversion and to tighten the resulting GPD uncertainty bands, especially near the kinematic region $x \simeq \xi$ where

the DVCS amplitude is most sensitive to the detailed GPD structure.

Because the integral transform operator and structural GPD constraints are implemented exactly, extending the architecture to simultaneously learn multiple GPDs is a straightforward modification of the output layer. The same replica strategy will yield a full probability distribution over the GPD quadruplet $(H, E, \tilde{H}, \tilde{E})$ as a function of (x, ξ, t, Q^2) .

The method is also well suited for performing combined fits to fixed-target and collider kinematics, as it does not assume a specific functional form for any GPD. This flexibility is particularly important in the kinematic region where fixed-target experiments probe large ξ at modest Q^2 , while collider measurements probe small ξ at larger Q^2 . A unified neural representation with a differentiable QCD evolution layer would enable a seamless description of both regimes.

C. Advantages and limitations of the present strategy

The differentiable PV inversion developed in this work offers several conceptual advantages over more traditional GPD extraction frameworks. By avoiding an explicit parametrization of $H^{(+)}(x, \xi, t, Q^2)$ in terms of double distributions, Regge ansätze, or truncated polynomial expansions, the method minimizes functional bias and allows the data to determine the x -, ξ -, t -, and Q^2 -dependence of the GPD within the kinematic support of the input CFF ensemble. All hard QCD structure is encoded in the fixed PV kernel and in the symmetry factors enforcing C-evenness and endpoint suppression, so the only additional information introduced by hand is the smoothness prior used to regularize the ill-posed inverse problem. In this sense, the reconstruction of $H^{(+)}$ is as close as possible to a direct, data-driven inversion of $\Re e \mathcal{H}$ rather than a fit within a restricted model class.

Strictly speaking, the endpoint factor $E(x) = (1 - |x|)^\beta$ is itself a mild but explicit structural prior: it enforces the physically expected vanishing of $H^{(+)}$ as $|x| \rightarrow 1$ and prevents the inversion from using the poorly constrained endpoint region to absorb discrepancies in $\Re e \mathcal{H}$. In practice, the exponent β controls the effective function class available to the optimizer: increasing β suppresses endpoint-supported modes (which the PV transform constrains only weakly) and can improve numerical stability, while too large a value can introduce bias by overly restricting the large- $|x|$ behavior. For this reason we treat β as a hyperparameter calibrated in closure studies alongside the curvature strength λ_x and the PV excision width, choosing values that minimize closure bias while avoiding spurious oscillations. A natural extension is to make β trainable (globally, or with a weak kinematic dependence) by parametrizing it as a positive quantity, e.g. $\beta = \text{softplus}(\tilde{\beta})$, and adding a gentle prior or penalty that keeps β within a physically reasonable range; in that case

the replica ensemble would also quantify sensitivity to endpoint assumptions rather than fixing them *a priori*. When $\Im m \mathcal{H}$ is included simultaneously with $\Re e \mathcal{H}$, the additional diagonal constraint at $x = \xi$ further reduces the null space of the inversion and correspondingly lessens the reliance on endpoint suppression and other stabilizing priors.

A second advantage is methodological. Because the PV transform is implemented as a differentiable layer inside the neural network, the entire mapping

$$(\xi, t, Q^2) \longrightarrow H^{(+)}(x, \xi, t, Q^2)$$

is trained end-to-end. This avoids the two-step procedures in which one first fits a CFF model and then infers a compatible GPD parametrization. In the present approach the same architecture simultaneously encodes the convolution kernel, the symmetry properties of the GPD, and the regularization in x , ξ , and t , while the Monte-Carlo replica ensemble propagates the full experimental covariance into the final $H^{(+)}$ band where the required CFF is determined in a purely data driven scheme prior to inversion. The result is a probabilistic GPD extraction with uncertainties that are straightforward to interpret as coming from the input CFF errors plus systematic variation in the priors.

The deliberate choice not to enforce positivity bounds, polynomiality moment constraints, or dispersion relations beyond those already implicit in the use of C-even combinations has both benefits and limitations. It avoids importing theoretical prejudices whose quantitative validity at current scales and kinematics is not always clear, and it provides a clean baseline against which the impact of such constraints can later be assessed. On the other hand, the reconstructed GPDs are not guaranteed to satisfy all known QCD consistency conditions exactly; mild violations of positivity or polynomiality may occur in regions where the experimental information is sparse or the inversion is most ill-conditioned. Moreover, the smoothness priors and network architecture themselves represent a controlled but nontrivial source of modeling, particularly when extrapolating beyond the region densely covered by CFF data.

The dominant limitation of the method is its sensitivity to the experimental uncertainty and modeling systematics in the input CFFs. Increasing the strength of smoothness priors (e.g., curvature penalties) stabilizes the ill-posed inversion by suppressing oscillatory modes, but it inevitably introduces bias by restricting the space of admissible GPD solutions. Robust application therefore requires systematic hyperparameter studies to balance CFF fidelity against regularization-induced bias. The most practical calibration step, as done here, is to invert the mean CFF and use the resulting GPD to define an analytic surrogate for closure testing; this helps ensure that tuning is performed in a physically relevant function class, although it does not remove methodological bias. The final GPD uncertainty and any residual bias are ultimately bounded by the quality of the CFF extraction, since sys-

tematic effects in the CFF model propagate directly into the reconstructed GPD.

A further practical limitation of any extraction based on $\Re e \mathcal{H}$ alone is that it constrains $H^{(+)}$ only through a singular PV integral, so the data primarily fix a smeared functional of the GPD and leave substantial degeneracy in the underlying x -dependence. A more interpretable and better constrained determination of H is achieved when $\Re e \mathcal{H}$ is used simultaneously with $\Im m \mathcal{H}$: at leading order $\Im m \mathcal{H}$ directly anchors the GPD on the cross-over line, $H^{(+)}(x = \xi, \xi, t, Q^2)$, while $\Re e \mathcal{H}$ constrains complementary principal-value information away from that line. Jointly fitting both components therefore reduces the null-space of the inversion, improves stability against noise, and yields uncertainty bands that more transparently reflect where the experimental observables genuinely constrain the x -shape of the GPD.

These considerations suggest a natural future extension in which the present, minimally constrained inversion serves as a baseline for systematically reintroducing additional QCD information. In particular, one can exploit the exact forward-limit relation $H^{(+)}(x, 0, 0) \rightarrow q(x) - \bar{q}(x)$ constrained by global fits to collinear PDFs, as well as the nucleon form-factor sum rules that relate the first x -moments of H and E to the quark contributions to the Dirac and Pauli form factors $F_1^q(t)$ and $F_2^q(t)$ [12]. Within the current method these inputs can be incorporated either as soft penalty terms in the loss function or as post-hoc consistency checks on the replica ensemble, rather than as hard constraints that dominate the fit. In this way one can quantify, in a controlled manner, how much each theoretical prior tightens the GPD band relative to the purely data-driven reconstruction reported here, and identify kinematic regions where existing constraints and experimental information are mutually compatible or in tension.

D. Conclusion

The differentiable inversion strategy developed here opens the door to a new class of flexible, uncertainty-quantified hadron structure extractions that remain tightly anchored to QCD factorization. By embedding the singular PV integral transform as a fixed, differentiable physics layer, the network is trained end-to-end in the GPD space while being constrained directly by the experimentally inferred CFF information. In practice, stability is achieved through a controlled balance between fidelity to the input CFFs and smoothness priors motivated by the ill-posed nature of the PV inversion, and closure studies provide a quantitative means to calibrate this balance and estimate methodological bias within the experimentally relevant phase space.

A key physics limitation is that DVCS at leading twist and leading order primarily constrains the C-even quark combination $H^{(+)}(x, \xi, t, Q^2) = H(x, \xi, t, Q^2) - H(-x, \xi, t, Q^2)$. Incorporating $\Im m \mathcal{H}$ together with $\Re e \mathcal{H}$

would substantially improve interpretability and stability, because $\Im m \mathcal{H}$ anchors the GPD on the cross-over line $x = \xi$ while $\Re e \mathcal{H}$ provides complementary principal-value information away from that line, reducing the null space of the inversion. However, even a simultaneous determination of $\Re e \mathcal{H}$ and $\Im m \mathcal{H}$ does not by itself separate the quark and antiquark pieces $H(x)$ and $H(-x)$ independently; in that stronger sense, obtaining “the full H ” generally requires additional external information and/or channels, such as forward-limit PDF constraints, form-factor sum rules, further DVCS polarization observables, or complementary processes, together with controlled theoretical priors.

With the arrival of large and precise DVCS datasets at accelerator facilities worldwide, GPD extractions will increasingly require methods that are both high-capacity and systematically improvable. The framework presented here provides a robust baseline: it preserves the analytic structure of QCD factorization while delivering a proba-

bilistic GPD reconstruction whose uncertainties can be traced to experimental CFF errors and to controlled regularization choices. This combination of physics-aware machine learning and rigorous uncertainty propagation represents a practical pathway toward fully multidimensional nucleon tomography from current and future data.

ACKNOWLEDGMENTS

The Deep Neural Network models used in this work were trained using the University of Virginia’s high-performance computing cluster, Rivanna. The authors acknowledge Research Computing at the University of Virginia for providing computational resources and technical support that have contributed to the results reported in this publication. URL: <https://rc.virginia.edu>. This work was supported by the DOE contract DE-FG02-96ER40950.

[1] D. Müller, D. Robaschik, B. Geyer, F. M. Dittes, and J. Horejsi, *Fortsch. Phys.* **42**, 101 (1994), [arXiv:hep-ph/9812448 \[hep-ph\]](https://arxiv.org/abs/hep-ph/9812448).

[2] A. V. Radyushkin, *Phys. Rev. D* **56**, 5524 (1997), [hep-ph/9704207](https://arxiv.org/abs/hep-ph/9704207).

[3] X. D. Ji, *Phys. Rev. D* **55**, 7114 (1997), [hep-ph/9609381](https://arxiv.org/abs/hep-ph/9609381).

[4] X. Ji, *Phys. Rev. Lett.* **78**, 610 (1997).

[5] J. C. Collins and A. Freund, *Phys. Rev. D* **59**, 074009 (1999), [hep-ph/9801262](https://arxiv.org/abs/hep-ph/9801262).

[6] X. Ji and J. Osborne, *Phys. Rev. D* **58**, 094018 (1998), [hep-ph/9801260](https://arxiv.org/abs/hep-ph/9801260).

[7] A. V. Belitsky and A. V. Radyushkin, *Phys. Rept.* **418**, 1 (2005), [hep-ph/0504030](https://arxiv.org/abs/hep-ph/0504030).

[8] P. C. Hansen, *Rank-Deficient and Discrete Ill-Posed Problems: Numerical Aspects of Linear Inversion* (Society for Industrial and Applied Mathematics, Philadelphia, PA, 1998).

[9] A. N. Tikhonov and V. Y. Arsenin, *Solutions of Ill-posed Problems* (Winston & Sons, Washington, DC, 1977) original Russian edition: Nauka, Moscow (1974).

[10] D. Müller, *Few Body Syst.* **55**, 317 (2014), [arXiv:1405.2817 \[hep-ph\]](https://arxiv.org/abs/1405.2817).

[11] M. Diehl, *Eur. Phys. J. C* **25**, 223 (2002), [arXiv:hep-ph/0205208 \[hep-ph\]](https://arxiv.org/abs/hep-ph/0205208).

[12] M. Diehl, *Phys. Rept.* **388**, 41 (2003), [arXiv:hep-ph/0307382 \[hep-ph\]](https://arxiv.org/abs/hep-ph/0307382).

[13] K. Kumerički and D. Müller, *EPJ A* **52**, 157 (2016), [1602.02763](https://arxiv.org/abs/1602.02763).

[14] M. Guidal, *EPJ A* **37**, 319 (2008), 0711.3743.

[15] H. Moutarde *et al.*, *EPJ C* **78**, 890 (2018), 1807.07620.

[16] K. Kumerički, D. Müller, and A. Schäfer, *Journal of High Energy Physics* **2011**, 73 (2011), [arXiv:1106.2808 \[hep-ph\]](https://arxiv.org/abs/1106.2808).

[17] M. Čuić, K. Kumerički, and A. Schäfer, *Physical Review Letters* **125**, 232005 (2020).

[18] H. Moutarde, B. Pire, L. Szymanowski, and J. Wagner, *EPJ C* **79**, 614 (2019), 1905.02089.

[19] L. Calero Díaz and D. Keller, *Physical Review D* **10.1103/PRD/sb63-sfdt** (2025), [arXiv:2509.18331 \[nucl-ex\]](https://arxiv.org/abs/2509.18331).

[20] R. D. Ball, L. Del Debbio, S. Forte, A. Guffanti, J. I. Latorre, A. Piccione, J. Rojo, and M. Ubiali, *Nuclear Physics B* **809**, 1 (2009).

[21] R. D. Ball, L. Del Debbio, S. Forte, A. Guffanti, J. I. Latorre, A. Piccione, J. Rojo, and M. Ubiali, *Nuclear Physics B* **816**, 293 (2009).

[22] R. D. Ball, V. Bertone, S. Carrazza, C. S. Deans, L. Del Debbio, S. Forte, A. Guffanti, N. P. Hartland, J. I. Latorre, J. Rojo, and M. Ubiali, *Nuclear Physics B* **867**, 244 (2013).

[23] T. N. Collaboration, R. D. Ball, V. Bertone, S. Carrazza, C. S. Deans, L. Del Debbio, S. Forte, A. Guffanti, N. P. Hartland, J. I. Latorre, J. Rojo, and M. Ubiali, *Journal of High Energy Physics* **2015**, 1 (2015), [arXiv:1410.8849 \[hep-ph\]](https://arxiv.org/abs/1410.8849).

[24] E. R. Nocera, R. D. Ball, S. Forte, G. Ridolfi, and J. Rojo, *Nuclear Physics B* **887**, 276 (2014).

[25] L. Del Debbio, T. Giani, J. Karpie, K. Orginos, A. Radyushkin, and S. Zafeiropoulos, *J. High Energ. Phys.* **02**, 138, [arXiv:2010.03996 \[hep-ph\]](https://arxiv.org/abs/2010.03996).

[26] H. Dutrieux, H. Moutarde, and P. Sznajder, *Eur. Phys. J. C* **82**, 300 (2022), [arXiv:2202.06888 \[hep-ph\]](https://arxiv.org/abs/2202.06888).

[27] X. Ji, *Journal of Physics G: Nuclear and Particle Physics* **24**, 1181 (1998).

[28] A. Radyushkin, *Physics Letters B* **449**, 81 (1999).

[29] M. V. Polyakov and C. Weiss, *Phys. Rev. D* **60**, 114017 (1999).

[30] P. V. Pobylitsa, *Phys. Rev. D* **67**, 034009 (2003).

[31] A. V. Radyushkin, *Phys. Rev. D* **59**, 014030 (1998).

[32] B. Pire, J. Soffer, and O. Teryaev, *Eur. Phys. J. C* **8**, 103 (1999).

[33] M. Diehl, T. Feldmann, R. Jakob, and P. Kroll, *Nuclear Physics B* **596**, 33 (2001).

[34] M. Diehl, T. Feldmann, R. Jakob, and P. Kroll, *Nuclear Physics B* **605**, 647 (2001).

[35] P. V. Pobylitsa, *Phys. Rev. D* **65**, 077504 (2002).

- [36] P. V. Pobylitsa, *Phys. Rev. D* **65**, 114015 (2002).
- [37] P. V. Pobylitsa, *Phys. Rev. D* **66**, 094002 (2002).
- [38] P. V. Pobylitsa, *Phys. Rev. D* **67**, 094012 (2003).
- [39] P. V. Pobylitsa, *Phys. Rev. D* **70**, 034004 (2004).
- [40] B. B. Le and D. Keller, arXiv preprint arXiv:2504.15458 [10.48550/arXiv.2504.15458](https://arxiv.org/abs/2504.15458) (2025), [arXiv:2504.15458](https://arxiv.org/abs/2504.15458) [cs.LG].
- [41] A. V. Belitsky and D. Müller, *Phys. Rev. D* **82**, 074010 (2010).
- [42] J. Ansel *et al.*, in *29th ACM International Conference on Architectural Support for Programming Languages and Operating Systems, Volume 2 (ASPLOS '24)* (ACM, 2024).
- [43] U. D. of Energy (USDOE), *A New Era of Discovery: The 2023 Long Range Plan for Nuclear Science*, Tech. Rep. (US Department of Energy (USDOE), Washington, DC (United States). Office of Science, 2023).
- [44] R. A. K. et al., Snowmass 2021 white paper: Electron ion collider for high energy physics (2022), [arXiv:2203.13199](https://arxiv.org/abs/2203.13199) [hep-ph].
- [45] E. C. Aschenauer, S. Fazio, K. Kumerički, and et al., *Journal of High Energy Physics* **2013**, 93 (2013).
- [46] A. A. et al., Electron ion collider: The next qcd frontier - understanding the glue that binds us all (2014), [arXiv:1212.1701](https://arxiv.org/abs/1212.1701) [nucl-ex].
- [47] K. Kumerički, D. Müller, and K. Passek-Kumerički, *Nuclear Physics B* **794**, 244 (2008).
- [48] M. Diehl and D. Ivanov, *Eur. Phys. J. C* **52**, 919 (2007).
- [49] K. Kumerički, D. Müller, and K. Passek-Kumerički, *Eur. Phys. J. C* **58**, 193 (2008).
- [50] H. W. Engl, M. Hanke, and A. Neubauer, *Regularization of Inverse Problems*, Mathematics and Its Applications, Vol. 375 (Kluwer Academic Publishers, Dordrecht, 1996).
- [51] D. Keller, arXiv preprint arXiv:2509.11456 (2025), [arXiv:2509.11456](https://arxiv.org/abs/2509.11456) [hep-ph].
- [52] I. P. Fernando and D. Keller, *Phys. Rev. D* **108**, 054007 (2023).
- [53] I. P. Fernando and D. Keller, arXiv preprint arXiv:2510.17243 [10.48550/arXiv.2510.17243](https://arxiv.org/abs/2510.17243) (2025), [arXiv:2510.17243](https://arxiv.org/abs/2510.17243) [hep-ph].